Unsteady propulsion and the acoustic signature of undulatory swimmers in and out of ground effect

Nathan Wagenhoffer **

Department of Engineering, Penn State Abington, Abington, Pennsylvania 19001, USA

Keith W. Moored and Justin W. Jaworski

Department of Mechanical Engineering and Mechanics, Lehigh University, Bethlehem, Pennsylvania 18015, USA



(Received 12 August 2019; accepted 4 March 2021; published 19 March 2021)

The propulsive performance and acoustic emission of undulatory swimmers are investigated using an integrated unsteady potential flow and acoustic boundary element solver. Anguilliform and carangiform swimming gaits are modeled by a deforming NACA 0012 airfoil section for various reduced frequencies and dimensionless wave numbers based on the body length. The most efficient swimming motions are achieved when the reduced frequency and dimensionless wave number are approximately equal, a condition which also minimizes the thrust, required power, and radiated acoustic pressure. A vertically oriented dipole dominates the transient acoustic response in the near and far fields for both classes of swimming gait. The effect of a ground plane on undulatory swimming and its associated noise generation is examined as a function of reduced frequency and altitude above the plane using the method of images. Ground effect becomes pronounced when swimming within half of a chord length from the ground plane, where the thrust, power, propulsive efficiency, and peak acoustic pressure all increase for both gaits. All swimming configurations simulated in this study experience positive period-averaged lift at proximal distances where increased thrust and other hydrodynamic performance benefits associated with ground effect occur.

DOI: 10.1103/PhysRevFluids.6.033101

I. INTRODUCTION

Many aquatic animals use traveling-wave motions of their bodies to propel themselves efficiently through the open ocean and near the ocean floor. From these undulatory motions, animals produce time-varying boundary layers over their bodies and shed a structured vortex wake. These flow features are important to animal propulsive forces and are also sources of flow-induced noise, where little is known about the flow-induced noise signature of aquatic animals [1]. Trailing edge noise generation has been studied for fixed foil geometries that may be either rigid [2-4] or compliant [5–7], where edge deformations due to local flow fields are allowed. However, recent numerical work has begun to shed light on the acoustics of pitching foils [8-10] and combined pitching and heaving foils [11]. These studies show that oscillating hydrofoils produce dipole acoustic emissions whose peak sound levels increase with Strouhal number (St = fA/U) and reduced frequency $(f^* = fc/U)$, where f is the frequency, A is the peak-to-peak amplitude, U is the flow speed, and c is the chord length. The Strouhal number can also be written as the product of the reduced frequency and the dimensionless amplitude as St = fA/c. Yet the acoustic signature of swimmers such as flatfish using whole-body traveling wave kinematics [12] has not been examined either far

^{*}nate.wagenhoffer@gmail.com

from or near a boundary such as the ocean floor. Moreover, the trade-off and connection between the performance and acoustic emissions of undulatory swimmers has not yet been investigated. The objective of this study is to provide insight into these limitations of our current knowledge, which can inform the design of high-performance, quiet bio-inspired underwater vehicles.

The swimming gaits of aquatic animals lie generally along an undulation-to-oscillation continuum [13] described parametrically by the dimensionless wave number formed by the ratio of the body or chord length to the wavelength of the motion, $k^* = c/\lambda$. Undulatory swimmers (e.g., eel, lamprey, and flatfishes) swim in an anguilliform mode characterized by $k^* \leq 1$ [12,14]. In contrast, oscillatory swimmers such as trout, mackerel, and tuna use subcarangiform, carangiform, and thunniform modes, respectively, that are generally characterized by $k^* > 1$ [15]. The thrust production and energetics of traveling-wave kinematics were first examined theoretically by a quasistatic model for elongated swimmers [16]. Although this theory can work well at low Reynolds numbers where viscous forces dominate, inertial forces dominate at high Reynolds numbers that are typical of many animals and must be included. This essential physical feature was recognized and incorporated into unsteady theories that were later developed for slender three-dimensional bodies [17,18] and two-dimensional wavy plates [19]. Further experimental and numerical work has examined the performance and flow physics of traveling-wave swimmers for the design of novel bio-inspired underwater vehicles [20–25].

Most research studies focused on the fluid mechanics of aquatic locomotion assume that the swimmer is in open water and far from any boundaries. Yet there are numerous animals that are benthic or near-ground swimmers, such as sole, flounder, halibut, and turbot, that exploit unsteady ground effect to improve their cost of transport or cruising speed [12,26–29]. Experimental and numerical studies of pitching and combined heaving-and-pitching hydrofoils have also demonstrated enhanced thrust production with no change in propulsive efficiency when operating in ground effect [30,31]. Moreover, these studies identified the existence of stable swimming altitudes above the ground plane where the period-averaged lift vanishes and any perturbation away from this equilibrium position produces a hydrodynamic restoring force. Although undulatory body motions constitute a better physical model of benthic swimmers than rigid pitching and heaving hydrofoils, there is little existing work that probes the performance and flow physics of swimmers using traveling-wave body motions in ground effect [32,33], and there is no published work to our best knowledge on their associated flow-induced acoustic signatures.

Motivated by these observations, the present work proceeds by addressing three unresolved research questions. How do the magnitude and directivity of the acoustic signature of a traveling-wave swimmer change with the relevant nondimensional variables far from the ground? What is the performance and wake structure of a traveling-wave swimmer in ground effect? How is the acoustic signature altered when a swimmer is in ground effect? To address these questions, the remainder of the paper is structured in the following manner. Section II describes the coupled potential flow and transient acoustic boundary element method used in this work. Section III introduces the *anguilliform* and *carangiform* traveling-wave swimming kinematics and frames the parameter space of the numerical simulations. Section IV discusses the limitations of the methodology presented. Section V presents results for the hydrodynamic performance, wake structures, and acoustic signatures of traveling-wave swimmers in free space and in ground effect. Conclusions and final remarks are presented in Sec. VI.

II. NUMERICAL METHODOLOGIES

A potential flow boundary element method is coupled to a transient acoustics boundary element method via Powell's acoustic analogy to compute all hydrodynamic and acoustic quantities in this work. The methodology and validation of the framework are presented in full detail by Wagenhoffer *et al.* [11,34]. An overview of the method is presented here and validation of the method is presented in the Appendix A. The potential flow solver is an adaptation of the panel method described by Willis *et al.* [35]. The inviscid flow around hydrofoils can be found by solving the Laplace equations

with an imposed no-penetration boundary condition on the body surface,

$$\nabla \phi \cdot \hat{\mathbf{n}} = 0 \text{ on } S_{b}, \tag{1}$$

where $\hat{\mathbf{n}}$ is the outward normal of the surface. The boundary integral equation integrates the effects of the combined distribution of sources and doublets on the body surface S_b and doublets on edge panel S_e , with vortex particles in the wake. The scalar potential may be written as

$$\phi(\mathbf{x}) = \int_{S_{h}} \left[\sigma(\mathbf{y}) G(\mathbf{x}, \mathbf{y}) - \mu(\mathbf{y}) \hat{\mathbf{n}} \cdot \nabla G(\mathbf{x}, \mathbf{y}) \right] dS - \int_{S_{e}} \mu_{e}(\mathbf{y}) \hat{\mathbf{n}} \cdot \nabla G(\mathbf{x}, \mathbf{y}) dS, \tag{2}$$

where **y** is a source position, **x** is the observer location, and $G(\mathbf{x}, \mathbf{y}) = \frac{1}{2\pi} \ln |\mathbf{x} - \mathbf{y}|$ is the two-dimensional Green's function for the Laplace equation. The source and doublet strengths are defined, respectively, as

$$\sigma = \hat{\mathbf{n}} \cdot (\mathbf{U} + \mathbf{U}_{\text{rel}} - \mathbf{U}_{\omega}),\tag{3}$$

$$\mu = \phi_i - \phi,\tag{4}$$

where \mathbf{U}_{ω} is velocity induced by the vortex particles in the field, \mathbf{U} is the body velocity, \mathbf{U}_{rel} is the velocity of the center of each element relative to the body frame of reference, and $\phi_i = 0$ is the interior potential of the body.

At each time step, vorticity is defined at the trailing edge to satisfy the Kutta condition. The trailing edge panel is assigned the potential difference between the upper and lower panels at the trailing edge of the foil, $\mu_e = \mu_{upper} - \mu_{lower}$, ensuring that the trailing edge of the hydrofoil has no bound circulation. Vorticity is represented in the computational domain by discrete, radially symmetric, desingularized Gaussian vortex particles. The induced velocity of the vortex blobs is evaluated by application of the Biot-Savart law, yielding [36]

$$\mathbf{U}_{\omega}(\mathbf{x},t) = \sum_{i=1}^{N} \frac{\Gamma_{i}}{2\pi} \left[1 - \exp\left(\frac{-|\mathbf{x} - \mathbf{y}|}{2r_{\text{cut}}^{2}}\right) \right], \tag{5}$$

where Γ is the circulation of the vortex particle and $r_{\rm cut}$ is the cutoff radius. Following the work of Pan *et al.* [37], the cutoff radius is set to $r_{\rm cut}=1.3\Delta t$ for time step Δt . By selecting this cutoff value, the wake particle cores overlap and create in effect a continuous, thin sheet of vorticity [38]. The cutoff radius needs to be minimal while maintaining vortex core overlap in order for the vortex wake to be convergent [39]. A larger cutoff radius could result in a region where the bound vorticity and shed vorticity cores overlap, resulting in a fictitious region of fluid that is less rotational. This numerical restriction on the vorticity accounted for in the fluid could lead to the wake observing less induced velocity than is physically warranted and thereby producing a "flatter" wake instead of something more akin to the reverse von Kármán vortex street anticipated. The evolution of the vortex particle position is updated using a forward Euler scheme [35]. The use of discrete vortices to represent the wake requires the use of two edge panels set behind the foil. The first edge panel, set with the empirical length of $l_{\rm panel}=0.4U_{\infty}\Delta t$ [40], satisfies the Kutta condition at the trailing edge. Next, the buffer panel is attached to the edge panel and stores information about the previous time step.

The induced velocity of the vortex particles on the body is accounted for in the definition of the source strength σ . The vortex particle induced velocity also augments the pressure calculation put forth by Katz and Plotkin [40]. The surface pressure is determined by

$$\frac{P_{f_{\infty}} - P_{f}(x)}{\rho} = \frac{\partial \phi_{\text{wake}}}{\partial t} \bigg|_{\text{body}} + \frac{\partial \phi}{\partial t} \bigg|_{\text{body}} - (\mathbf{U} + \mathbf{U}_{\text{rel}}) \cdot (\nabla \phi + \mathbf{U}_{\omega}) + \frac{1}{2} |\nabla \phi + \mathbf{U}_{\omega}|^{2}, \tag{6}$$

where $\partial \phi_{\text{wake}}/\partial t = \Gamma \dot{\theta}/(2\pi)$ is the time rate of change due to a vortex particle with circulation Γ at an angle θ from the observation point, and ρ is the fluid density. The pressure found on the body in

(6) is similar to the form put forth by Willis *et al.* [35], but here $\partial \phi_{\text{wake}}/\partial t$ is the positional change of a vortex with respect to a panel and does not require the solution of a secondary system to find the influence of wake vortices onto the body surface.

The Powell acoustic analogy, a derivative of the Lighthill acoustic analogy, uses vorticity as the forcing function to the wave equation [41]. The Powell acoustic analogy allows the vorticity determined by the flow solver to be the forcing function of the acoustic solver. The analogy states that in free space the forcing of the wave equation is a function of the vorticity in the field:

$$\partial_t^2 P_{\mathbf{a}} - \nabla^2 P_{\mathbf{a}} = \nabla \cdot (\boldsymbol{\omega} \times \mathbf{u}), \tag{7}$$

$$\frac{\partial G}{\partial n} = 0 \quad \text{on} \quad S_{\text{b}}. \tag{8}$$

Using a Green's function solution, and applying an integration by parts, the pressure in the field can be determined by

$$P_{\mathbf{a}}(\mathbf{x},t) = \rho \int_{S_{\mathbf{b}}} (\boldsymbol{\omega} \times \mathbf{u}) \cdot \frac{\partial G}{\partial n_{\mathbf{y}}} dS, \tag{9}$$

where $\partial G/\partial n_y$ is the Green's function for two-dimensional potential flow, n_y is the outward normal at the source with a corresponding outward normal at the observer n_x , \mathbf{u} is the velocity field, and $\boldsymbol{\omega} = \nabla \times \mathbf{u}$ is the vorticity. The pressure integral (9) applies regardless of whether or not a solid body is present [42]. For all of the flow scenarios examined in this work, the speed of sound ensures compact interactions of field vorticity with the body, allowing for the use of the potential flow Green's function to define the acoustic loading. Additionally, Euler's equation is arranged to define the acoustic dipole value necessary to guarantee a no-flux condition on the surface of the discrete geometry,

$$\rho \frac{\partial \mathbf{u}}{\partial t} = -\nabla P_{\mathbf{a}}.\tag{10}$$

The velocity vector in (10) is the normal induced velocity from all discrete vortices in the domain, including the discrete vortex particles that compose the wake and vortex values found along the foil, which are solved for in (2). A rearrangement of (10) that considers the outward normal pressure on the foil results in

$$\frac{\partial P_{\mathbf{a}}}{\partial n}(\mathbf{x}) = -\rho \sum_{i=0}^{N} \frac{\partial [\mathbf{u}_{i} \cdot \hat{\mathbf{n}}(\mathbf{x})]}{\partial t}.$$
 (11)

The acoustic pressure and its derivative found in Eqs. (9) and (11) define, respectively, the Dirichlet and Neumann boundary conditions of the Burton-Miller formulation for two-dimensional boundary element acoustics using the pressure definition $P_a = -\rho_0 \frac{\partial \Phi_a}{\partial t}$. The Burton-Miller formulation is commonly implemented as it is free of fictitious resonances [43]. The Burton-Miller formulation avoids the nonuniqueness associated with external acoustics boundary elements, making it suitable for wideband subsonic foil acoustics [44]. The Burton-Miller formulation is

$$\int_{S_{k}} \left[\frac{\partial G_{\kappa}(\mathbf{x}, \mathbf{y})}{\partial n} \phi_{a}(\mathbf{y}) + \frac{1}{2} \phi_{a}(\mathbf{y}) \right] dS + \beta \int_{S_{k}} \frac{\partial^{2} G_{\kappa}(\mathbf{x}, \mathbf{y})}{\partial n_{v} \partial n_{v}} \phi_{a}(\mathbf{y}) dS = \phi(x) + \beta \frac{\partial \phi(\mathbf{x})}{\partial n}, \quad (12)$$

where $G_{\kappa}(\mathbf{x}, \mathbf{y}) = iH_0^{(1)}(\kappa |\mathbf{x} - \mathbf{y}|)/4$ is the two-dimensional acoustic Green's function, κ is the acoustic wave number, ϕ_a is the associated acoustic potential, and $\beta = i/\kappa$ is a chosen coupling parameter. This selected value of β follows from the work of Wolf [45]. The solution to the frequency domain problem (12) produces a transient solution by application of the convolution quadrature method [34,46,47]. The convolution quadrature method allows Eqs. (9) and (11) to remain in their transient form, preserving any nonlinear interactions that occur due to body kinematics or the wake evolution.

A. Time discretization

The frequency potential operators found in the Burton-Miller formulation (12) are evaluated as convolution integrals. The Laplace transforms of the potential operators are convolved with an associated potential field. The potential field is evaluated by a convolution quadrature. The quadrature has an associated weight that is defined by a power series. This methodology of time discretization can be achieved via a convolution quadrature method put forth by Lubich [46]:

$$V * \Phi(t) = \int_0^t v(t - \tau)\phi(\tau) d\tau.$$

Here V represents a Laplace transform of the v operator, a characteristic differential operator of the transient wave equation, ϕ is some known potential distribution, and the operator * represents a convolution integral. For problems with a form similar to (12), the acoustic frequency Green's function is convolved with a transient potential solution that can be discretized in a similar manner to

$$v(t-\tau) * \phi(\tau)(\mathbf{x}) = \int_{S_b} V(\mathbf{x} - \mathbf{x}', t-\tau)\phi(\tau) d\mathbf{x}'. \tag{13}$$

Splitting the time domain into N+1 time steps of equal spacing, $\Delta t = T/N$ and $t_n = n\Delta t$ for n = [0, 1, ..., N], the discrete convolution can be viewed as

$$v * \phi(n\Delta\tau)(\mathbf{x}) \approx \sum_{i=0}^{n} \omega_{n-j}(\Delta t)\phi(j\Delta t). \tag{14}$$

The convolution weights, ω , are determined via the following:

$$\omega_{n-j}(\Delta t) = \frac{1}{2\pi i} \oint_C \frac{V\left[\frac{\gamma(\xi)}{\Delta t}\right]}{\xi^{j+1}} d\xi, \tag{15}$$

where C is a circle of radius $\lambda < 1$ centered at the origin. A second-order backwards difference function, $\gamma(\xi) = (1 - \xi) + \frac{1}{2}(1 - \xi)^2$, describes the time step, where ξ is a substitute for the spatial variable. Employing a scaled inverse transform, the weights become

$$V\left[\frac{\gamma(\xi)}{\Delta t}\right] = \sum_{n=0}^{\infty} \omega_{n-j} \xi^n, \quad |\xi| < 1, \tag{16}$$

$$\omega_{n-j}^{\Delta t,\lambda}(V) = \frac{\lambda^{-j}}{N+1} \sum_{\nu=0}^{N} V(\eta) \xi_{N+1}^{y_j}, \tag{17}$$

with

$$\xi_{N+1} = \exp\left(\frac{2\pi i}{N+1}\right),\tag{18}$$

$$s_l = \gamma \left(\lambda \xi_{N+1}^{-l}\right) / \Delta t,\tag{19}$$

being the quadrature spacing of time and the accompanying time-dependent complex wave number that is generated. The value of s_l is different for each time step and provides the link between the frequency-domain solver and a transient boundary integral equation such as (12). For this formulation $\lambda = \Delta t^{3/N}$ is selected based on the error analysis of Banjai and Sauter [48].

B. Grid independence

Convergence studies on the number of boundary elements and time steps are performed for a carangiform swimming gait with a reduced frequency of $f^* = 0.5$. Figure 1 shows spatial (a) and temporal (b) convergence for the sum of the acoustic potential on the body over four cycles of

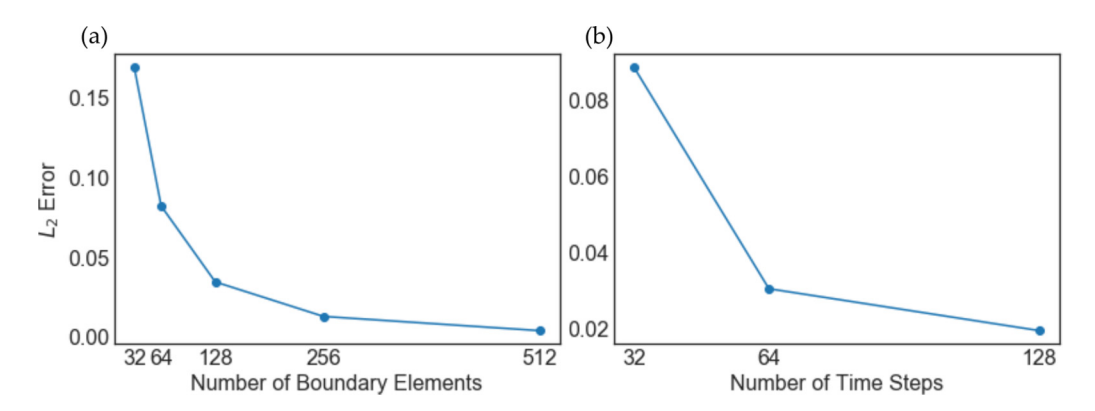


FIG. 1. Spatial and temporal convergence of coupled BEM. (a) The convergence rate of the acoustic potential over the body as the number of boundary elements on the body doubles for a fixed number of time steps. (b) The convergence rate of the acoustic potential over the body as the number of time steps per cycle doubles for a fixed number of boundary elements.

motion. The root-mean-squared (RMS) percent error is found for a doubling of boundary elements with the acoustic pressure of a 1024 element system used as the base value. The spatial convergence was conducted for a fixed temporal resolution of 256 time steps per period. The acoustic pressure changes by less than 1% for 256 boundary elements in comparison to the 1024 element solution. The temporal convergence study used a fixed number of 256 body elements. Figure 1(b) indicates a 2% change in force when increasing the number of time steps per period of motion from 128 to 256. A further doubling of time steps was conducted, but erroneous results were produced in the potential flow solver for 512 time steps per cycle of motion. All of the simulation results presented previously used 150 time steps per period of motion and 256 boundary elements to define the discrete body. The previous work conducted by Wagenhoffer *et al.* [34] showed spatial and temporal convergence for the solver when 150 boundary elements and 256 time steps per cycle were employed.

III. PROBLEM FORMULATION

Undulatory fish locomotion is normally modeled by traveling-wave body deformations [19,20,25]. Anguilliform and carangiform waveforms are examined in the present work as a basis for the undulatory swimming motion of many fish species. The free-swimming model defined in the work of Maertans *et al.* [25] was simplified to define a waveform for the kinematic model employed here. A deformable NACA 0012 hydrofoil, with its leading edge of the neutral axis fixed at the origin, is subjected to a lateral displacement h(x, t) for any point x along the foil at time t,

$$h(x,t) = a_0 A(x) \sin \left[2\pi (kx - ft) \right], \tag{20}$$

$$A(x) = a_1 + a_2 x + a_3 x^2, (21)$$

where A(x) is the envelope of the traveling wave with coefficients a_1 , a_2 , and a_3 describing the shape of the displacement, k is the wave number, f is the frequency, and a_0 is the amplitude at the trailing edge. The space and time constants have been nondimensionalized by the chord length c and the freestream velocity U_{∞} , respectively. The anguilliform gait [14] and carangiform gait [49] are, respectively, characterized by coefficients:

anguilliform
$$a_1 = 0.367$$
, $a_2 = 0.323$, $a_3 = 0.310$, carangiform $a_1 = 0.2$, $a_2 = -0.825$, $a_3 = 1.625$,

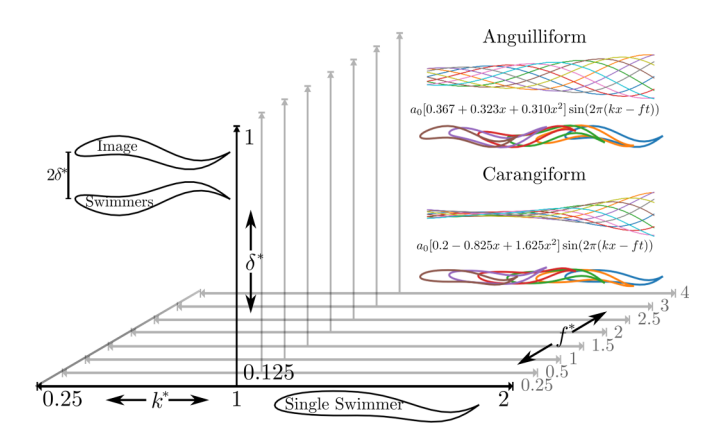


FIG. 2. Parameter space used in the single swimmer and ground effect studies conducted in this work. Each study is performed for both the anguilliform and carangiform gaits depicted in the top-right corner. The single swimmer study is subjected to a variation of wave number $(0.25 \le k^* \le 2)$ and frequency $(0.25 \le f^* \le 4)$. The image swimmer study has a fixed wave number $(k^* = 1)$ and varies the distance to the ground plane $(0.125 \le \delta^* \le 1)$ and frequency $(0.25 \le f^* \le 4)$. For the choice of unit chord and freestream velocity, the values of k, f, and δ are the same as k^* , f^* , and δ^* , respectively.

where the dimensions of these coefficients are such to render A(x) a dimensionless function. A trailing edge amplitude of $a_0/c = 0.1$ is selected for all simulations, matching the amplitude selected by Maertans *et al.* [25], who note a drag minimization at this amplitude for moderate and high reduced frequencies in their viscous simulations.

Figure 2 illustrates the parameter space of the anguilliform and carangiform waveforms. The displacements of the neutral axis and of the entire foil due to traveling-wave deformations are shown over a period of motion T in the top-right corner of the figure. The anguilliform gait is characterized by displacement along the entire chord length, while the carangiform gait exhibits notable displacements mainly from the midchord to trailing-edge region.

The simulations results presented where produced by a NACA 0012 foil discretized into 256 elements distributed spatially with a cosine function to ensure a greater density of elements at the leading and trailing edges of the foil. The swimming gaits where simulated for eight cycles of motion discretized into 150 equal spaced time steps. The last four swimming cycles are used to define the Dirichlet and Neumann boundary conditions [Eqs. (10) and (11), respectively] on the right-hand side of the Burton-Miller formulation (12).

The undulatory swimming studies are parameterized by the dimensionless wave number $k^* = kc$, the reduced frequency $f^* = fc/U$, and the Strouhal number $\mathrm{St} = fa_0/U$. One typical undulatory ground effect swimmer, plaice (*Pleuronectes platessa*), has the characteristic dimensionless values of $k^* \approx 1$, $f^* \approx 2$, and $\mathrm{St} \approx 0.23$ [12], which are used to inform the ranges of each parameter. The reduced frequency range is $0.25 \leqslant f^* \leqslant 4$, which for fixed $a_0/c = 0.1$ corresponds to a Strouhal number range of $0.025 \leqslant \mathrm{St} \leqslant 0.4$. The single-swimmer study varies f^* in this range and the dimensionless wave number over $0.25 \leqslant k^* \leqslant 2$, as indicated on the horizontal plane in Fig. 2.

Simulations for traveling-wave swimmers in ground effect are conducted using the method of images. The distance of the swimmer to the ground plane δ introduces an additional dimensionless parameter, $\delta^* = \delta/c$. The ground effect simulations vary the swimmer distance from the ground over the range $0.125 \le \delta^* \le 1$. The ground effect swimmer is subjected to the same reduced frequency range as the single swimmer but at a fixed dimensionless wave number, $k^* = 1$. This parameter space for the ground effect study is illustrated by the vertical plane in Fig. 2.

The potential flow solver can also determine the associated performance characteristics of these oscillating foils. The force acting on the foil is defined by $\mathbf{F} = -\int_{S_b} P_f \hat{\mathbf{n}} dS$, where P_f is the pressure from the flow solver as opposed to the acoustic pressure, $\hat{\mathbf{n}}$ is the local outward normal vector,

and S_b is the foil surface. Since the potential flow method is inviscid, the forces on the foil arise only from its external pressure distribution. The power consumption of the oscillating motion is calculated as the negative inner product of the force and velocity vectors of each boundary element, i.e., $P_w = -\int_{S_b} \mathbf{F}_{ele} \cdot \mathbf{u}_{ele} dS$. The variables \mathbf{F}_{ele} and \mathbf{u}_{ele} refer to the force and velocity acting on each element, respectively. The time-averaged coefficients of lift, thrust, and power may be defined as

$$C_L = \frac{\overline{F}_y}{\frac{1}{2}\rho U_\infty^2}, \quad C_T = -\frac{\overline{F}_x}{\frac{1}{2}\rho U_\infty^2}, \quad C_P = \frac{\overline{P}_w}{\frac{1}{2}\rho U_\infty^3}, \tag{22}$$

where F_x and F_y are the integrated streamwise and transverse components of the force on the foil, respectively. The propulsive efficiency is defined as $\eta = C_T/C_P$.

The acoustic pressure field for each swimming configuration is computed on a circle with a radius 50 chord lengths centered on the midchord of the foil. The RMS pressure is then calculated at each discrete point on the circle over four cycles of foil motion. A nondimensional acoustic pressure $P^* = 2P/\rho U^2$ is used throughout this work. The simulations are carried out over eight cycles of motion to remove any transient effects that would occur in either the hydrodynamic metrics or the resulting acoustic fields.

IV. MODEL LIMITATIONS

The coupled fluid-acoustic model put forward assumes the dominant noise producing mechanism of fish swimming is body-vortex interactions. This assumption ignores noise-generating mechanisms such as boundary layer noise generation or leading edge separation. The numerical fluid model assumes that the flow is attached, as is typical in fish swimming [50]. All vorticity imparted to the flow by the body is due to trailing-edge vortex shedding to satisfy the Kutta condition. Ground effect swimming is modeled with the method of images, which implicitly ignores any boundary layer formation or effects on the ground plane. However, potential flow solutions have been shown to match experiments well for foils operating within a quarter-chord of the ground plane [30,51]. Leading edge, dorsal, and anal fin vortex shedding phenomena are neglected, which may be important for some fish. The present model further assumes two-dimensional flow and therefore neglects any tip vortex generation. Both fin-fin interaction and three-dimensional flow are two extensions that can be developed for this method.

It is further noted that the vortex particle model in the present numerical scheme does not include a diffusion or vortex spreading method. The simulations indicate that the majority of acoustic loading from the wake is due to the most recently shed vortex, where the vorticity is in closest proximity to the body. Diffusion of this vorticity would be minimal in the short time period since its production at the trailing edge.

V. RESULTS

A. Isolated swimmer

Figure 3 presents the wake structures for both the anguilliform and carangiform swimmers for $k^* = 1.125$ and $f^* = 1.5$. The wakes are similar and form reverse von Kármán vortex streets, both of which have been observed previously in the context of undulating swimmers [52]. One subtle difference is that the carangiform swimmer's wake has a greater wake deformation in the cross-stream direction than the anguilliform swimmer. This differentiation suggests that the carangiform swimmer has stronger cross-stream velocities, greater energy wasted into the wake, and a lower propulsive efficiency than the anguilliform swimmer, which is in agreement with previous work [52] and the calculated efficiency presented later in Fig. 6.

Figure 4 presents the near-field transient acoustic pressure for only the anguilliform swimmer, without loss of generality, since both gaits produce qualitatively similar acoustic fields. The acoustic field is measured around the perimeter of circles centered on the midchord of the swimmer with

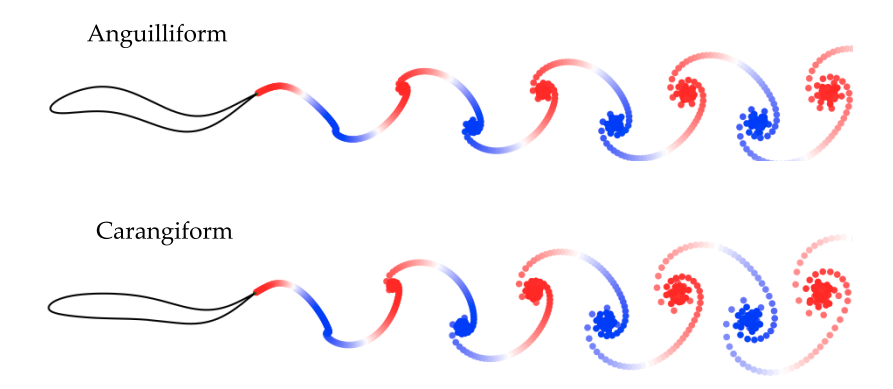


FIG. 3. Comparison of the wakes produced by an anguilliform (top) and a carangiform (bottom) gait for wave number $k^* = 1.125$ and reduced frequency $f^* = 1.5$.

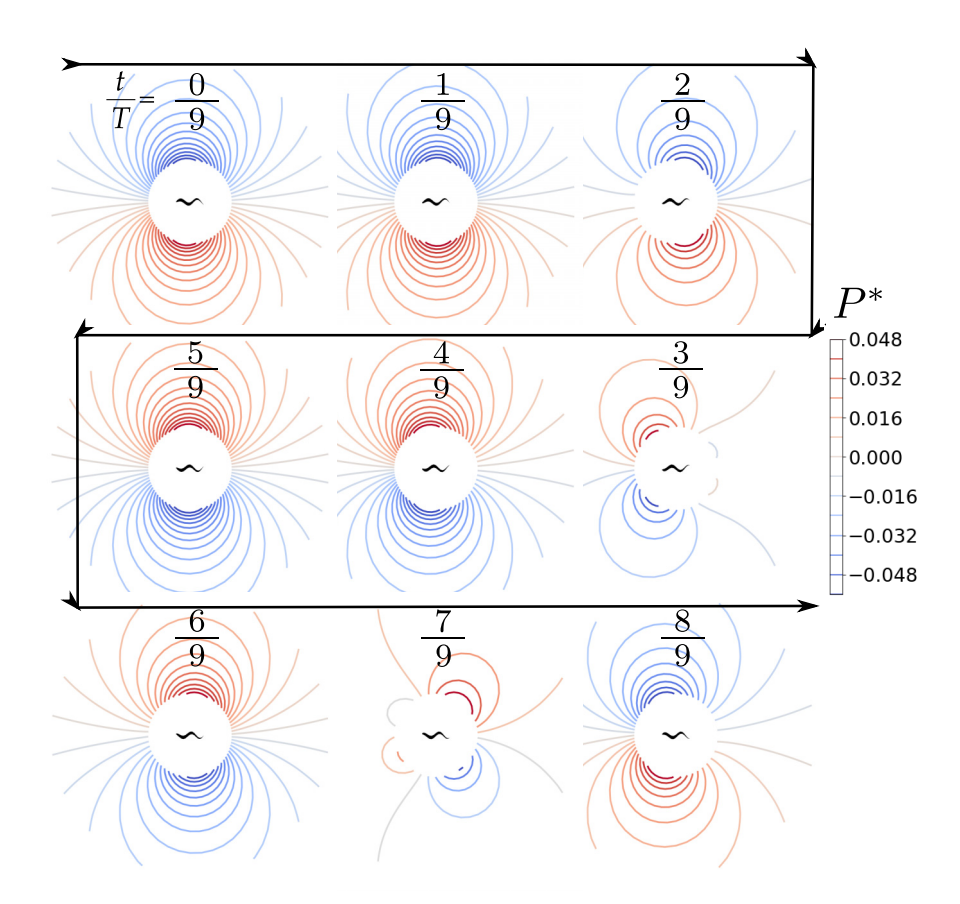


FIG. 4. Acoustic near field of a typical traveling wave swimmer. Transient acoustic response of an anguilliform swimmer at $f^* = 1$ and $k^* = 1$. The near field begins two chord lengths from the midchord and is extended to five chord lengths away. One period of traveling wave motion is shown from $t/T = 0/9 \rightarrow 8/9$.

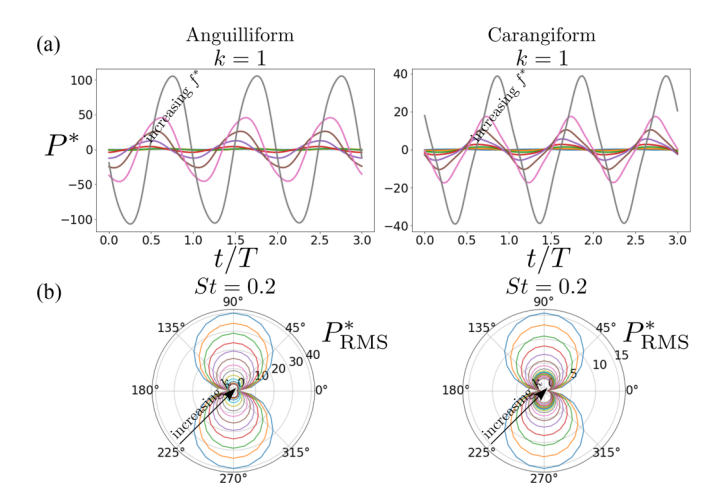


FIG. 5. Transient and time-averaged far-field acoustic responses of traveling wave swimmers. (a) Transient acoustic pressure found 50 chord lengths above the midchord of an anguilliform and carangiform gait swimmers at $k^* = 1$. For fixed wave number, the acoustic pressure increases with Strouhal number. (b) RMS acoustic pressure of anguilliform and carangiform gait swimmer at Strouhal number $St^* = 0.2$ found around a circle 50 chord lengths away from the midchord. The RMS acoustic pressure decreases as the wave number increases for fixed reduced frequency.

radii varying from two to five chord lengths. The acoustic response is shown over a single period of traveling wave motion with $f^* = 1$ and $k^* = 1$. The directivity is generally a vertically oriented dipole, except at times t/T = 3/9 and 7/9 when a quadrupole response is observed. The trailing edge of the swimmer is transitioning from the upstroke to the downstroke (or vice versa) at these times, coinciding with a sign change in the bound circulation and therefore the acoustic loading. The quadrupole is formed when two weaker acoustic lobes in the directivity pattern begin to form at the leading edge of the swimmer, as the stronger preceding acoustic lobes move to the trailing edge of the swimmer. The acoustic pressure maximum travels from the leading edge to the trailing edge as the period progresses.

The far-field acoustic pressure is measured for all swimming configurations in a similar manner to the near field, but at a radius of 50 chord lengths. Figure 5(a) shows the transient acoustic pressure response directly above the midchord of the foil over three cycles of anguilliform and carangiform gait motions with a wave number $k^* = 1$. The plot shows that the acoustic pressure emitted from a swimmer with fixed wave number increases with the Strouhal number or reduced frequency. Figure 5(b) shows the time-averaged acoustic pressure P^*_{RMS} on the circle 50 chords from the foil for both anguilliform and carangiform gaits with St = 0.2. A vertically oriented dipole directivity is observed for the time-averaged pressure field for all swimming parameters considered. Since the directivity is the same for all swimmers, the peak RMS acoustic pressure can be used as a single value to describe the acoustic field. The peak RMS acoustic pressure P^*_{Peak} decreases as the wave number increases for a fixed Strouhal number.

Figure 6(a) shows the peak RMS acoustic pressure as a function of the reduced frequency and wave number. The peak RMS acoustic pressure is minimized when $k^* \approx f^*$ for both gaits in a thrust-producing regime. The minimum of P_{Peak}^* corresponds with the peak efficiency in the thrust-producing regime, which could be a result of the majority of swimming power being translated into thrust, not lift. However, it should be noted that the minimum peak acoustic pressure does not always occur at peak efficiency as observed in the case of combined heaving and pitching foils [11,53]. The region $f^* < k^*$ produces the minimum peak RMS acoustic pressure across all values explored but corresponds to a drag regime. The acoustic directivity produced by both swimming gaits has the

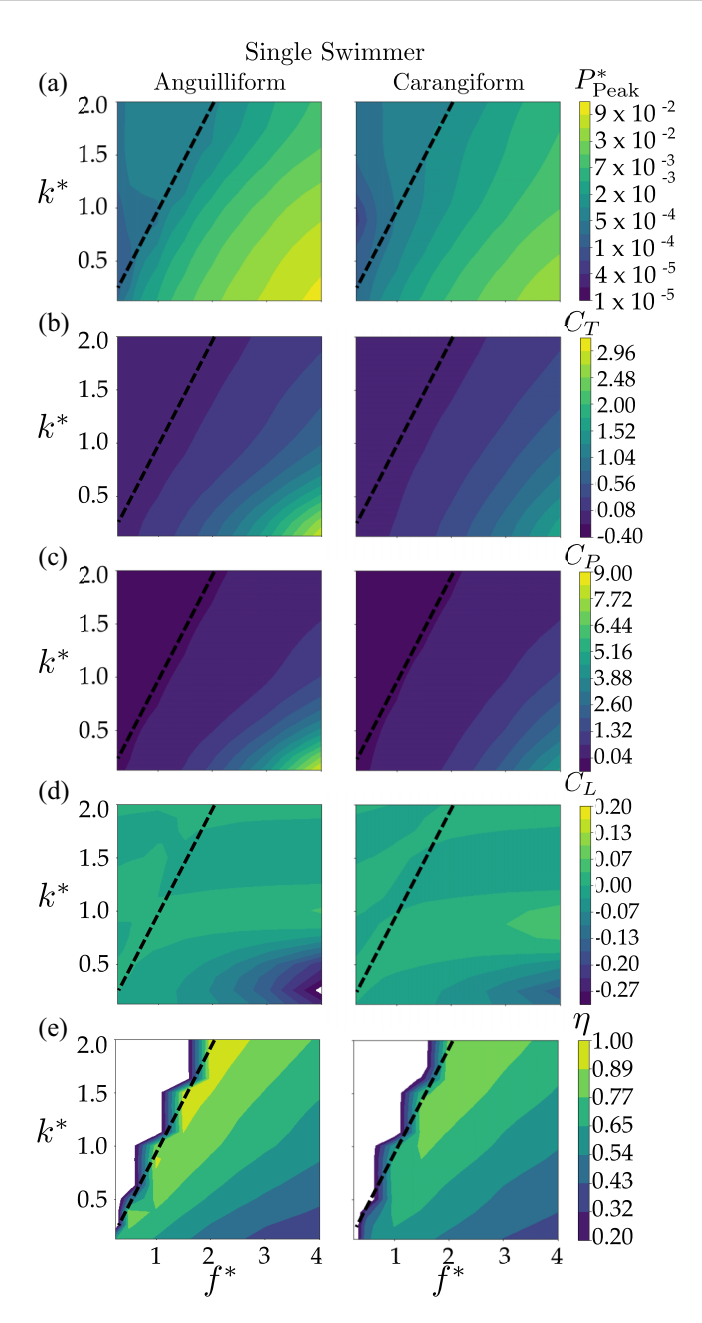


FIG. 6. Acoustic and hydrodynamic performance metrics of isolated traveling wave swimmers. Metrics are shown for both anguilliform and carangiform gaits as functions of reduced frequency f^* and wave number k^* . (a) Peak RMS acoustic pressure P^*_{Peak} , (b) coefficient of thrust C_T , (c) coefficient of power C_P , (d) coefficient of lift C_L , and (e) efficiency η . The dashed black lines indicate where $k^* = f^*$. The white regions of (e) indicate the drag-producing regime.

same vertical orientation as a lift dipole, even though the coefficient of lift approaches zero in the $k^* \approx f^*$ region. The region $f^* > k^*$ sees a similar trend to that of coefficients of power and thrust, with the peak RMS acoustic pressure increasing as the ratio $f^*/k^* > 1$ grows.

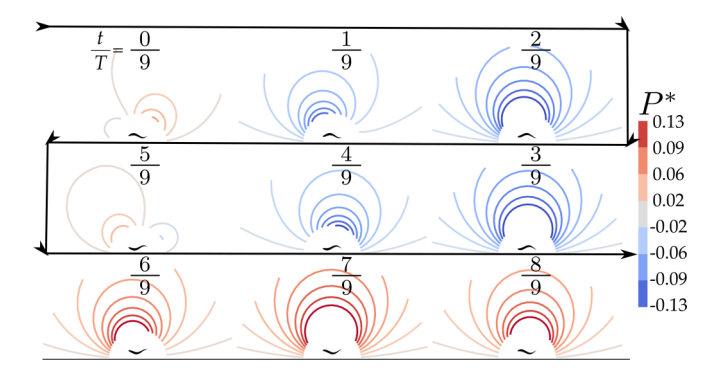


FIG. 7. Transient near acoustic field of an anguilliform swimmer in ground effect for $f^* = 2$, $k^* = 1$, and $\delta^* = 0.25$. The acoustic field is found from two chord lengths to five chord lengths from the ground plane over a period of motion T, as indicated by the arrow going from t/T = 0/9 to 8/9.

Figure 6 shows that there are similar trends for both gaits in the coefficients of thrust, power, and lift, and the efficiency as the wave number and reduced frequency vary. The anguilliform gait does, in general, produce higher thrust, power, and lift magnitude than the carangiform gait when operating at the same wave number and reduced frequency. The efficiency is also higher for the anguilliform gait with a maximum efficiency $\eta=0.94$, while the carangiform gait's maximum efficiency is $\eta=0.86$. The maximum efficiency of both gaits is found when $f^*\approx k^*$, which is the same result derived from potential flow theory for a linearly increasing traveling wave amplitude envelope [19]. The white regions of the efficiency graphs are drag producing and are omitted. In Fig. 6(b) it can be seen that the thrust coefficient approaches zero for $f^*\approx k^*$ and is negative (drag producing) when the wave number is less than the reduced frequency $f^*< k^*$. In the region where the reduced frequency is greater than wave number $(f^*>k^*)$ the coefficient of thrust increases with the ratio f^*/k^* . The power coefficient follows similar trends as the thrust coefficient with the minimum power coefficient, in a thrust-producing regime, occurring when $f^*\approx k^*$.

B. Ground effect swimming

To model the effect of an animal swimming near the ocean floor on the hydrodynamics and acoustics, the method of images is employed [30]. The ideal swimmer for the ground effect studies has a caudal fin planform that is parallel to the ground during rectilinear swimming motions resulting in the peak of the acoustic dipole produced penetrating the ocean floor. The method of images is a classical technique that computes the hydrodynamic and acoustic fields for two bodies oscillating out of phase in free space (cf. Fig. 2). At the symmetry plane between the two bodies, the cross-stream velocity will be exactly canceled, satisfying the no-flux condition and thereby modeling an inviscid ground plane. The symmetry plane also imposes a cancellation of acoustic velocity there, while the bottom (image) body *generates* the acoustic pressure wavefront that is the reflection of the interaction of the acoustic pressure from the top body with the symmetry plane. The coupled boundary element framework is specifically developed to account for the hydrodynamic and acoustic interactions between multiple bodies and can therefore be used to model ground effect swimming in this manner.

Figure 7 illustrates the acoustic near field for a period of motion for an anguilliform swimmer at $f^* = 2$, $k^* = 1$, and at a distance $\delta^* = 0.25$. It should be noted that the swimming motion begins with an upstroke of the trailing edge at t/T = 0/9 and switches to a downstroke at t/T = 5/9. Two pressure lobes observed at each of these times indicate a quadrupolar response similar to the directivity of an isolated swimmer when changing stroke direction. However, a negative or positive lobe dominates the acoustic field during the upstroke or downstroke, respectively. The far-field

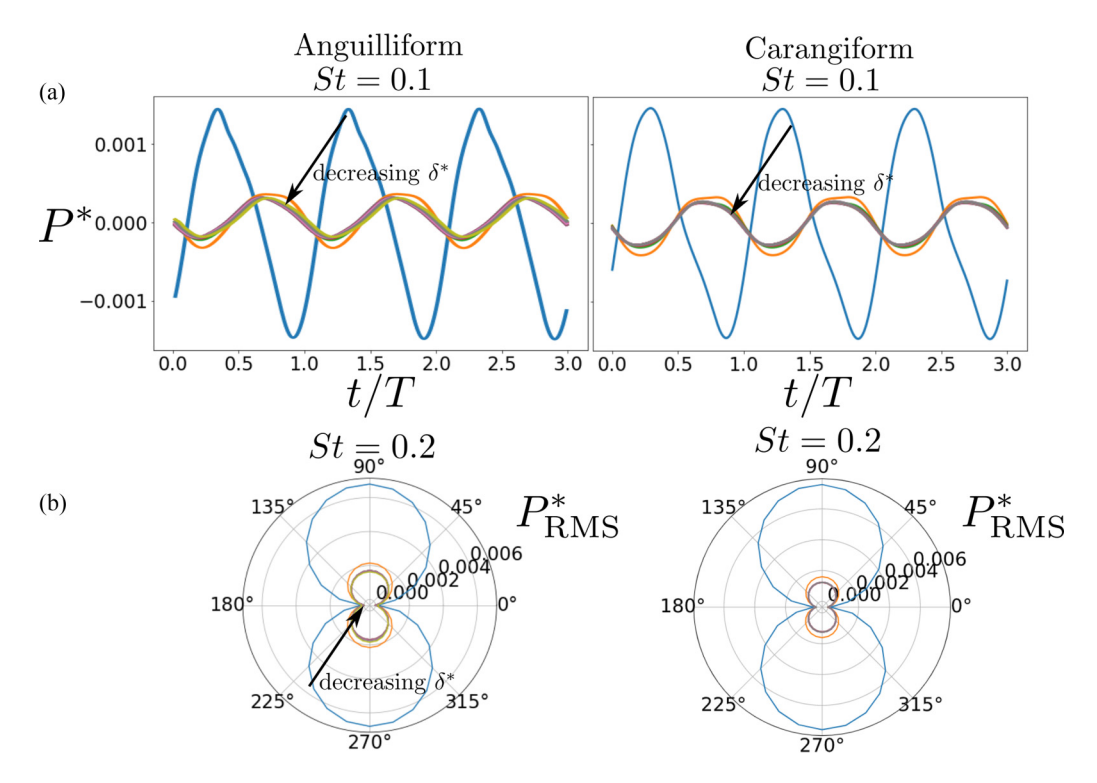


FIG. 8. Transient and time-averaged acoustic responses of traveling wave swimmers in ground effect. (a) Transient acoustic pressure found 50 chords above the ground plane about the midchord of anguilliform and carangiform gait swimmers in ground effect at Strouhal number of $St^* = 0.1$. The distances of $\delta^* = 0.125$ (blue line) and $\delta^* = 0.1875$ (orange line) are labeled, while all other distances $\delta^* \geqslant 0.25$ overlap. (b) Directivity plot of the RMS acoustic pressure of anguilliform and carangiform gait swimmers with $St^* = 0.2$ along a circle centered about the midpoint between the swimmer and its image in the ground.

acoustic pressure is computed around a circle 50 chord lengths from the origin located on the ground plane between the midchords of the image swimmers. Figure 8 shows the transient and time-averaged acoustic output of swimmers in ground effect. Figure 8(a) shows that the greatest acoustic pressure is produced by the swimmer at a distance of $\delta^* = 0.125$ (blue line) and the acoustic pressure recovers to that of a swimmer far from the ground by the distance $\delta^* = 0.3$ (gray line). This trend is the same for both gaits across all frequencies studied. Note that the acoustic responses are not sinusoidal due to the nonlinear dynamics of the wake vortices. Figure 8(b) shows the entire directivity field of a ground effect anguilliform and carangiform swimmers at St = 0.2, even though only the upper half plane is the region of physical interest. The directivity is the same dipole shape as the isolated swimmer in Fig. 5(b). Once again, the similar shape of the RMS acoustic pressure across all ground effect swimmers allows the peak RMS acoustic pressure P_{Peak}^* to be used as the single metric to describe the acoustic output. Figure 9 shows the hydrodynamic and acoustic performance metrics of anguilliform and carangiform gaits swimming as a function of the distance from a ground plane and the reduced frequency. Figure 9(a) shows that the peak RMS acoustic pressure becomes a strong function of f^* when $\delta^* \ge 0.3$ and is invariant to changes in δ^* in this region. However, when $\delta^* < 0.3$ the effect of the ground becomes pronounced and the acoustic pressure is amplified as δ^* decreases.

Figure 10 presents the wake vorticity field shed from an anguilliform swimmer with a wave number $k^* = 1$ and a reduced frequency of $f^* = 3$ as a function of the ground proximity. Figure 10(a) shows the amplification of bound circulation as the proximity to the image swimmer is increased. A

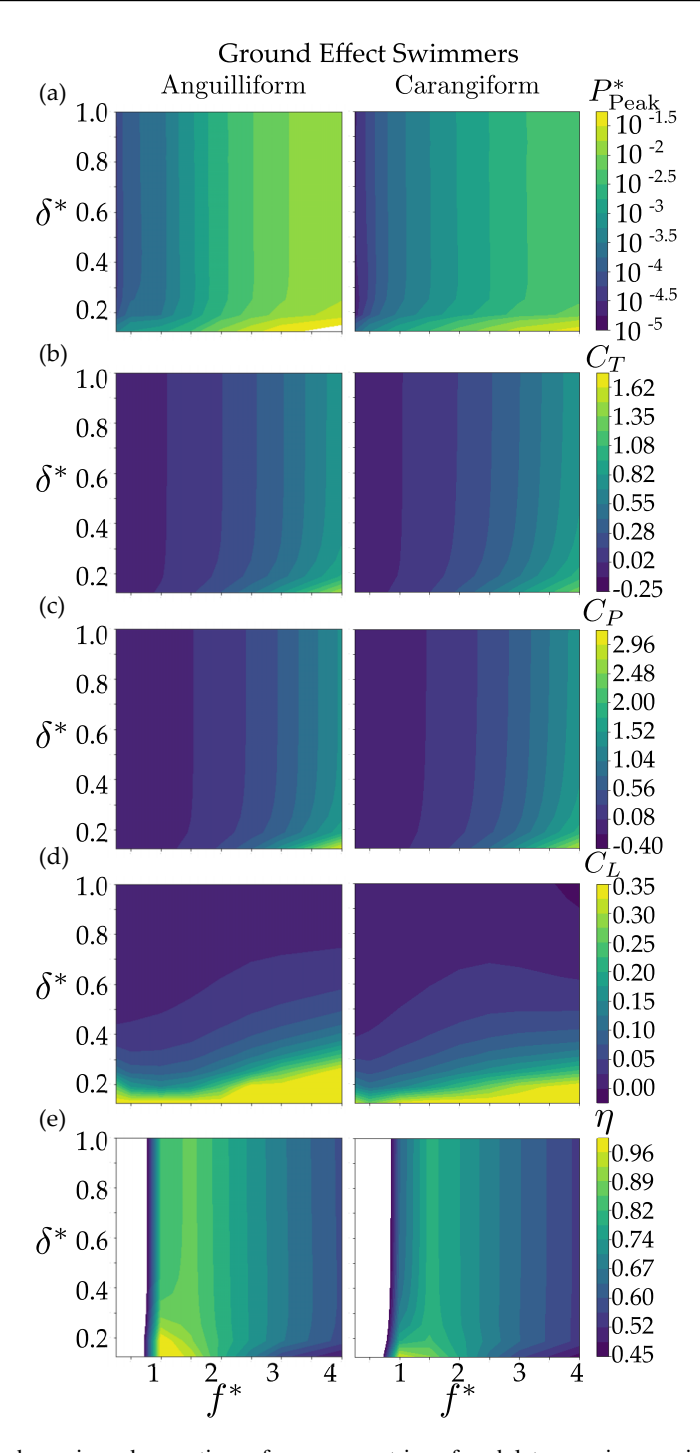


FIG. 9. Hydrodynamic and acoustic performance metrics of undulatory swimmers in ground effect as a function of the nondimensional distance to the ground plane and reduced frequency. The left column shows the results for an anguilliform gait, and the right column is for a carangiform gait. (a) Peak RMS acoustic pressure, (b) thrust coefficient, (c) power coefficient, (d) lift coefficient, and (e) propulsive efficiency. The white regions of (e) indicate the drag-producing regime.

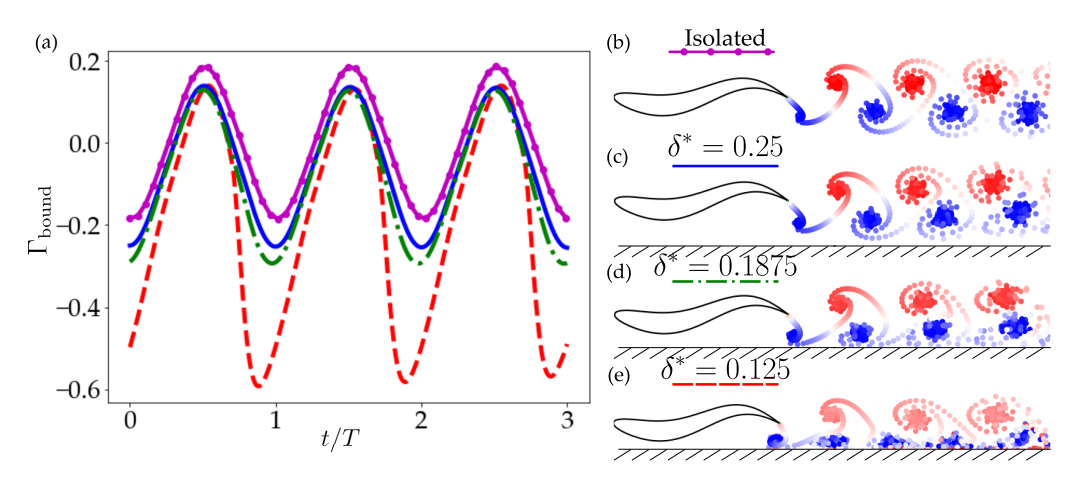


FIG. 10. Examples of the bound circulation and wake formation from anguilliform gait swimming near an inviscid solid boundary. (a) Total bound circulation on the swimmer over three cycles of motion for anguilliform swimmers operating at a wave number of $k^* = 1$ and a reduced frequency of $f^* = 3$ due to varying distances from the ground plane. The top swimmer of the right column (b) depicts the wake produced by an isolated swimmer. Descending the right column depicts the wakes produced by a swimmer as it travels closer to the ground plane: (c) $\delta^* = 0.25$, (d) $\delta^* = 0.1875$, and (e) $\delta^* = 0.125$.

reduction of δ^* corresponds with an increase in force production, which is observed in both the lift and thrust coefficients in Figs. 9(b) and 9(d). The increase in force production by the swimmer also corresponds with an increase in the peak RMS acoustic pressure. As the swimmer moves closer to the ground plane, the wake region near the trailing edge becomes drawn upstream and underneath the body due to the influence of the image wake. The variation of the wake production due to distance from the ground plane is observed in Figs. 10(b)-10(e). The wake in Fig. 10(b), due to an isolated swimmer, is entirely aft of the swimmer. The wake begins to be drawn under the swimmer by $\delta^* = 0.1875$ [cf. Fig. 10(d)] and is drawn in farther as the foil distance to the ground decreases [cf. Fig. 10(e)]. Similar wake deformations have been observed for experiments and potential flow simulations of pitching foils in ground effect [30], where viscous interactions with the ground plane were shown to have little effect on the large-scale vortex structures predicted in potential flow models.

For swimmers within a distance $\delta^* < 0.5$ to the ground plane, Fig. 9 indicates an increase in the lift, power, and thrust coefficients, efficiency, and peak RMS acoustic pressure with decreasing δ^* . For distances of $\delta^* > 0.5$, all of these metrics are essentially independent of changes in δ^* , with the exception of the coefficient of lift. Figure 11 presents contours of the lift coefficient as a function of δ^* and f^* , which indicates that there is an equilibrium altitude (denoted by the red dashed line) where the lift force is zero. For δ^* below and above the dashed line there is a positive lift and negative lift force, respectively, acting to push the swimmer towards a stable equilibrium altitude. Equilibrium altitudes were first reported for pitching foils in ground effect [30] and were later reported in other studies [31,33]. For reduced frequencies $f^* > 1$, the anguilliform gait has an equilibrium position that is farther from the wall than the carangiform gait. The equilibrium altitudes always lie outside of the region where there is any significant amplification of acoustic pressure or hydrodynamic forces for the swimming scenarios considered in this work. This behavior is likely due to the low-amplitude swimming used in the current study, and the exploration of large-amplitude swimming motions is the subject of ongoing research that is beyond the scope of the present work.

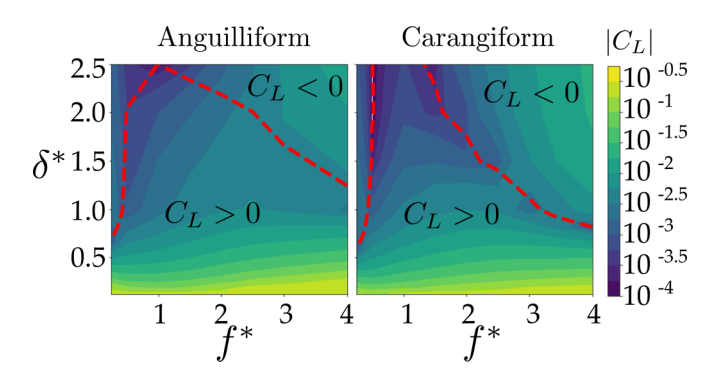


FIG. 11. Equilibrium altitude of ground effect swimmers. Logarithmic heat maps of the lift coefficient of swimmers in ground effect are shown as a function of the ground distance and reduced frequency. The region in which the period-averaged lift coefficient transitions from positive to negative is denoted by a dashed red line.

VI. CONCLUSION

A unified unsteady potential flow/acoustic boundary element method is used to computationally investigate the propulsive performance and acoustic emission of undulatory swimming. Anguilliform and carangiform swimming gaits are assessed over a range of reduced frequencies and wave numbers. The most efficient swimming motions have a dimensionless wave number that is approximately the value of the reduced frequency, which consequently corresponds with a minimization of acoustic pressure, thrust, and power. The thrust and power increase with the ratio of the reduced frequency to the dimensionless wave number. The directivity of the transient acoustic near field of both swimming gaits is dominated by a vertically oriented dipole, where a quadrupole directivity occurs transiently as the trailing edge of the swimmer switches from upstroke to downstroke or vice versa. The dipolar directivity of the period-averaged far-field acoustic pressure for all scenarios considered allows the peak RMS acoustic pressure to be the sole metric for noise level comparisons. The peak RMS acoustic pressure increases with reduced frequency but decreases when the dimensionless wave number increases.

Swimming in ground effect is modeled by the method of images for both swimming gaits across varying reduced frequencies and ground proximities. Increases in thrust, power, lift, efficiency, and peak acoustic pressure occur for both swimming gaits within half of a chord length of the ground plane. However, for distances greater than half of a chord length, the propulsive and acoustic performance of the foils recovers to that of an isolated swimmer far from the ground, with the exception of the lift. Stable equilibrium altitudes above the ground plane are identified at which the period-averaged lift is zero, and perturbations away from this altitude result in hydrodynamic restoring forces that return the swimmer to equilibrium. For the swimmers investigated in this study, the equilibrium altitudes occurred at ground proximities greater than what is required to gain the hydrodynamic performance benefits, such as increased thrust, that are associated with ground effect swimming.

ACKNOWLEDGMENTS

The authors gratefully acknowledge financial support from the National Science Foundation under grants 1653181 (K.W.M.) and 1805692 (J.W.J.), the Office of Naval Research under MURI grant N00014-08-1-0642 (K.W.M.), and a Lehigh CORE grant (J.W.J., K.W.M.).

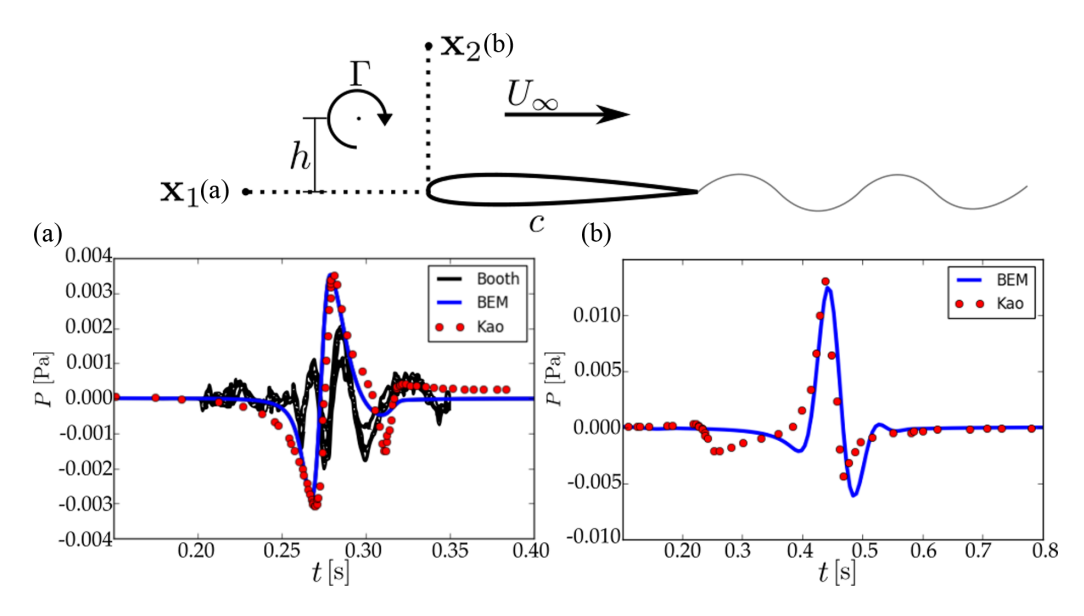


FIG. 12. Acoustic emission due to a single vortex advecting past a NACA 0012 airfoil. The vortex circulation Γ , chord length c, observation point x, freestream velocity U_{∞} , and offset heights h are different for each of the two validation cases. The response of (a) is observed 100 chord lengths in front of the foil $\mathbf{x}_1 = (0, 100c)$, while the response of (b) is observed 50 chord lengths above the airfoil $\mathbf{x}_2 = (0, 50c)$. The black lines represents the experimental results of Ref. [54], the red circle represents the matched asymptotic solution of Ref. [55], and the blue line is the result of the coupled potential flow and transient acoustics BEM put forward in this work.

APPENDIX

The Appendix is supplied to show the validation of the Powell acoustic analogy as a suitable forcing function for the coupled flow-acoustic BEM as first presented in Wagenhoffer *et al.* [11]. The experimental work of Booth [54] details acoustic scattering due to vortex-body interaction. The matched asymptotic method of Kao [55] uses this experimental study to validate their analysis. Kao asymptotically matches the acoustic loading from a potential flow solver to an outer far-field acoustic solution. The selected vortex-body interaction problem sets a vortex upstream of a NACA 0012 airfoil, with a chord of c = 0.2032 m. The vortex has a circulation of $\Gamma = 0.52$ m² s⁻¹ and advects in a freestream of speed $U_{\infty} = 4.7$ m s⁻¹ at a vertical displacement of h = 0.152c from the foil centerline (cf. Fig. 12). This particular offset distance was selected because at other distances in the experimental study the vortex impinges on the body and breaks down. The fluid medium has a speed of sound of $c_0 = 343$ m s⁻¹ and the density $\rho_0 = 1.225$ kg m⁻³. The acoustic response is then found in front of the airfoil at $\mathbf{x}_1 = (100c, 0)$, as shown in the problem schematic at the top of Fig. 12.

Figure 12(a) compares the experimental vortex-body interaction sound results from the work of Booth, the matched asymptotic method of Kao, and the coupled potential flow and acoustic BEM presented in this study. The matched asymptotic method and the flow-acoustic BEM have qualitatively similar responses. The experimental acoustic response is the same order of magnitude as the other methodologies with similar qualitative trends, albeit with more fluctuations in its signal. The leading edge acoustic response occurs at $t \approx 0.25$ s. It can be seen that the amplitude of this interaction is quantitatively similar for the theoretical and BEM approaches, while qualitatively the slope of the leading-edge response as it approaches the minimum pressure from the flow-acoustic BEM is steeper than the matched asymptotic method response. The trailing-edge acoustic response occurs at $t \approx 0.30$ s, where the peak predicted response of $P_a \approx -0.0015$ Pa from the matched

asymptotic solution is stronger than the BEM prediction of $P_{\rm a}\approx -0.0005$ Pa. The increased pressure response at the trailing edge from the matched asymptotic method can be affected by the Kutta condition and the manner in which the wake evolves behind the foil. Howe [56] stated that, as a vortex passes the trailing edge of a body, the vorticity shed into the wake tends to cancel the effect of the incoming vorticity and mitigates the noise generation. The Kutta condition in the potential flow BEM could be implicitly imposing the mechanism described by Howe, which would help explain the weaker acoustic response predicted by the flow-acoustic BEM framework. Additionally, the acoustic response in Fig. 12(a) is measured in front of the foil, a location where the acoustic pressure would be small in comparison to other measurement locations.

Further verification of the the flow-acoustic BEM is accomplished by measuring the acoustic response where it has its maximum value. Figure 12(b) presents the measurement of the acoustic response above the foil where the peak acoustic pressure occurs. The flow scenario has a vortex with circulation $\Gamma = 0.1 \,\mathrm{m}^2 \,\mathrm{s}^{-1}$ that is released five chord lengths upstream with the vertical offset h = 0.1c above the center of a NACA 0012 foil with chord c = 1 m. The case has a freestream velocity $U_{\infty} = 1 \,\mathrm{m \, s^{-1}}$, a sound speed of $c_0 = 5 \,\mathrm{m \, s^{-1}}$, and density $\rho = 1 \,\mathrm{kg \, m^{-3}}$. The acoustic response was measured 50 chord lengths above the leading edge of the foil at $\mathbf{x}_2 = (0, 50c)$. The matched asymptotic method predicts a leading-edge acoustic response at $t \approx 0.25$ s, which occurs before the flow-acoustic BEM response at $t \approx 0.35$ s. However, both approaches exhibit a similar magnitude of response. The maximum acoustic responses of both systems are found at $t \approx 0.45$ s with a pressure of $P_a = 0.013$ Pa. The trailing-edge responses at $t \approx 0.5$ s also exhibits similar magnitudes for both approaches, while the flow-acoustic BEM has a slightly longer unloading at t = 0.02 s than the matched asymptotic method. The flow-acoustic BEM predicts the same orderof-magnitude acoustic response as the experiments of Booth [54]. In addition, the flow-acoustic BEM produces qualitatively and quantitatively similar acoustic responses to the matched asymptotic method of Kao [55].

^[1] R. R. Fay, Fish Bioacoustics (Springer, New York, 2009), pp. 1851–1860.

^[2] J. E. Ffowcs Williams and L. H. Hall, Aerodynamic sound generation by turbulent flow in the vicinity of a scattering half plane, J. Fluid Mech. 40, 657 (1970).

^[3] A. A. Oberai, F. Roknaldin, and T. J. R. Hughes, Computation of trailing-edge noise due to turbulent flow over an airfoil, AIAA J. 40, 2206 (2002).

^[4] M. Roger and S. Moreau, Back-scattering correction and further extensions of Amiet's trailing-edge noise model. Part 1: Theory, J. Sound Vib. 286, 477 (2005).

^[5] J. W. Jaworski and N. Peake, Aerodynamic noise from a poroelastic edge with implications for the silent flight of owls, J. Fluid Mech. 723, 456 (2013).

^[6] A. V. G. Cavalieri, W. R. Wolf, and J. W. Jaworski, Numerical solution of acoustic scattering by finite perforated elastic plates, Proc. R. Soc. London A 472, 20150767 (2016).

^[7] J. W. Jaworski and N. Peake, Aeroacoustics of silent owl flight, Annu. Rev. Fluid Mech. 52, 395 (2020).

^[8] Y. Bae and Y. J. Moon, Aerodynamic sound generation of flapping wing, J. Acoust. Soc. Am. 124, 72 (2008).

^[9] A. Manela, On the acoustic radiation of a pitching airfoil, Phys. Fluids 25, 071906 (2013).

^[10] M. S. U. Khalid, I. Akhtar, and B. Wu, Quantification of flow noise produced by an oscillating hydrofoil, Ocean Eng. 171, 377 (2019).

^[11] N. Wagenhoffer, K. W. Moored, and J. W. Jaworski, On the noise generation and unsteady performance of combined heaving and pitching foils, arXiv:2101.09546 [physics.flu-dyn] (2021).

^[12] P. W. Webb, Kinematics of plaice, *Pleuronectes platessa*, and cod, *Gadus morhua*, swimming near the bottom, J. Exp. Biol. **205**, 2125 (2002).

^[13] M. Sfakiotakis, D. M. Lane, and J. B. C. Davies, Review of fish swimming modes for aquatic locomotion, IEEE J. Oceanic Eng. 24, 237 (1999).

- [14] E. D. Tytell, The hydrodynamics of eel swimming II. Effect of swimming speed, J. Exp. Biol. **207**, 3265 (2004).
- [15] G. V. Lauder and E. D. Tytell, Hydrodynamics of undulatory propulsion, Fish Physiol. 23, 425 (2005).
- [16] G. I. Taylor, Analysis of the swimming of long and narrow animals, Proc. R. Soc. London A 214, 158 (1952).
- [17] M. J. Lighthill, Hydromechanics of aquatic animal propulsion, Annu. Rev. Fluid Mech. 1, 413 (1969).
- [18] M. J. Lighthill, Note on the swimming of slender fish, J. Fluid Mech. 9, 305 (1960).
- [19] T. Yao-Tsu Wu, Swimming of a waving plate, J. Fluid Mech. 10, 321 (1961).
- [20] M. S. Triantafyllou and G. S. Triantafyllou, An efficient swimming machine, Sci. Am. 272, 64 (1995).
- [21] G. V. Lauder, E. J. Anderson, J. Tangorra, and P. G. A. Madden, Fish biorobotics: Kinematics and hydrodynamics of self-propulsion, J. Exp. Biol. 210, 2767 (2007).
- [22] B. P. Epps, P. V. Alvarado, K. Youcef-Toumi, and A. H. Techet, Swimming performance of a biomimetic compliant fish-like robot, Exp. Fluids 47, 927 (2009).
- [23] J. Yu, M. Wang, M. Tan, and J. Zhang, Three-dimensional swimming, IEEE Robot Automat. Mag. 18, 47 (2011).
- [24] K. W. Moored, P. A. Dewey, M. C. Leftwich, H. Bart-Smith, and A. J. Smits, Bioinspired propulsion mechanisms based on manta ray locomotion, Mar. Technol. Soc. J. 45, 110 (2011).
- [25] A. P. Maertens, M. S. Triantafyllou, and D. K. P. Yue, Efficiency of fish propulsion, Bioinspir. Biomim. 10, 046013 (2015).
- [26] R. W. Blake, Mechanics of gliding in birds with special reference to the influence of the ground effect, J. Biomech. **16**, 649 (1983).
- [27] P. W. Webb, The effect of solid and porous channel walls on steady swimming of steelhead trout *Oncorhynchus mykiss*, J. Exp. Biol. **178**, 97 (1993).
- [28] B. N. Nowroozi, J. A. Strother, J. M. Horton, A. P. Summers, and E. L. Brainerd, Whole-body lift and ground effect during pectoral fin locomotion in the northern spearnose poacher (*Aagonopsis vulsa*), Zoology 112, 393 (2009).
- [29] E. Blevins and G. V. Lauder, Swimming near the substrate: A simple robotic model of stingray locomotion, Bioinspir. Biomim. **8**, 016005 (2013).
- [30] D. B. Quinn, K. W. Moored, P. A. Dewey, and A. J. Smits, Unsteady propulsion near a solid boundary, J. Fluid Mech. 742, 152 (2014).
- [31] A. Mivehchi, J. Dahl, and S. Licht, Heaving and pitching oscillating foil propulsion in ground effect, J. Fluids Struct. **63**, 174 (2016).
- [32] D. B. Quinn, G. V. Lauder, and A. J. Smits, Flexible propulsors in ground effect, Bioinspir. Biomim. 9, 036008 (2014).
- [33] B. Kim, S. G. Park, Wei-Xi Huang, and H. J. Sung, An autonomous flexible propulsor in a quiescent flow, Int. J. Heat Fluid Flow 68, 151 (2017).
- [34] N. Wagenhoffer, K. W. Moored, and J. W. Jaworski, Accelerated acoustic boundary element method and the noise generation of an idealized school of fish, in *FLINOVIA II: Flow Induced Noise and Vibration Issues and Aspects*, edited by E. Ciappi, S. De Rosa, F. Franco, J.-L. Guyader, S. A. Hambric, R. C. K. Leung, and A. D. Hanford (Springer, New York, 2019), pp. 157–178.
- [35] D. J. Willis, J. Peraire, and J. K. White, A combined pFFT-multipole tree code, unsteady panel method with vortex particle wakes, Int. J. Numer. Methods Fluids 53, 1399 (2007).
- [36] G.-H. Cottet and P. D. Koumoutsakos, *Vortex Methods: Theory and Practice* (Cambridge University Press, Cambridge, 2000).
- [37] Y. Pan, X. Dong, Q. Zhu, and D. K. P. Yue, Boundary-element method for the prediction of performance of flapping foils with leading-edge separation, J. Fluid Mech. 698, 446 (2012).
- [38] P. Koumoutsakos and A. Leonard, High-resolution simulations of the flow around an impulsively started cylinder using vortex methods, J. Fluid Mech. 296, 1 (1995).
- [39] J. T. Beale, On the accuracy of vortex methods at large times, in *Computational Fluid Dynamics and Reacting Gas Flows* (Springer, New York, 1988), pp. 19–32.
- [40] J. Katz and A. Plotkin, Low-Speed Aerodynamics (Cambridge University Press, Cambridge, 2001).
- [41] A. Powell, Theory of vortex sound, J. Acoust. Soc. Am. 36, 177 (1964).

- [42] T. Kambe, Acoustic emissions by vortex motions, J. Fluid Mech. 173, 643 (1986).
- [43] S. Marburg, The Burton and Miller method: Unlocking another mystery of its coupling parameter, J. Comput. Acoust. 24, 1550016 (2016).
- [44] W. R. Wolf and S. K. Lele, Wideband fast multipole boundary element method: Application to acoustic scattering from aerodynamic bodies, Int. J. Numer. Methods Fluids 67, 2108 (2011).
- [45] W. R. Wolf, Airfoil Aeroacoustics, LES and Acoustic Analogy Predictions (Stanford University Press, Stanford, CA, 2011).
- [46] C. Lubich, Convolution quadrature revisited, BIT Numer. Math. 44, 503 (2004).
- [47] M. Hassell and F. J. Sayas, Convolution quadrature for wave simulations, in *Numerical Simulation in Physics and Engineering* (Springer, New York, 2016), pp. 71–159.
- [48] L. Banjai and S. Sauter, Rapid solution of the wave equation in unbounded domains, SIAM J. Numer. Anal. 7, 227 (2011).
- [49] J. J. Videler and F. Hess, Fast continuous swimming of two pelagic predators, saithe (*Pollachius virens*) and mackerel (*Scomber scombrus*): A kinematic analysis, J. Exp. Biol. **109**, 209 (1984).
- [50] E. J. Anderson, W. R. McGillis, and M. A. Grosenbaugh, The boundary layer of swimming fish, J. Exp. Biol. 204, 81 (2001).
- [51] M. Kurt, J. Cochran-Carney, Q. Zhong, A. Mivehchi, D. B. Quinn, and K. W. Moored, Swimming freely near the ground leads to flow-mediated equilibrium altitudes, J. Fluid Mech. 875, R1 (2019).
- [52] A. P. S. Maertens, Fish swimming optimization and exploiting multi-body hydrodynamic interactions for underwater navigation, Ph.D. thesis, Massachusetts Institute of Technology, 2015.
- [53] N. Wagenhoffer, Characterization of the Noise Generation from Biological and Bio-Inspired Swimmers with a Novel Fluid-Acoustic Numerical Framework, Ph.D. thesis, Lehigh University, 2019.
- [54] E. R. Booth, Experimental observations of two-dimensional blade-vortex interaction, AIAA J. 28, 1353 (1990).
- [55] H. C. Kao, Body-vortex interaction, sound generation, and destructive interference, AIAA J. 40, 652 (2002).
- [56] M. S. Howe, The influence of vortex shedding on the generation of sound by convected turbulence, J. Fluid Mech. **76**, 711 (1976).